



# Efficient real-time positioning using Bayesian analysis and magnetic anomaly field

Łukasz Jankowski\*, Dominik Pisarski, Robert Konowrocki, Błażej Popławski, Rami Faraj

*Institute of Fundamental Technological Research, Polish Academy of Sciences, Pawińskiego 5B, 02-106 Warsaw, Poland*

## ARTICLE INFO

### Keywords:

Sensor fusion

Bayesian inference

Real-time positioning

Magnetic anomaly

Intelligent navigation system

## ABSTRACT

Despite the prevalence of well-established and explored navigation systems, alternative localization methods are currently the focus of intensive research. This interest is driven by geopolitical challenges and increasingly sophisticated applications of mobile robots and uncrewed aerial vehicles. This study investigates the problem of real-time positioning in GPS-denied environments. Based on the mapped magnetic anomaly field and using Bayesian formalism for data fusion, the localization obtained from embedded sensors is corrected to reduce cumulative errors. The proposed method has minimal computational cost and a minimal number of tunable parameters. The paper introduces it and demonstrates its effectiveness in a laboratory study. Experimental tests, using a system equipped with an Inertial Measurement Unit, demonstrated a significant reduction in localization uncertainty. The improvement was especially notable in areas with large, smooth variations in the magnetic field. Finally, the accuracy of the method is analyzed, and its performance is compared to a particle filter.

## 1. Introduction

The Global Positioning System (GPS) is the essential element of many positioning, navigation, and timing services. It finds applications both in military operations and daily civilian activities. Given the extensive propagation distances that signals traverse from satellites to GPS receivers, the propagation environment can substantially influence signal strength and positioning accuracy. GPS signals are frequently obstructed in areas such as narrow valleys, lengthy tunnels, or urban environments characterized by densely distributed tall structures. Within an indoor environment, the GPS signal commonly experiences attenuation by a factor of 10 to 100 [1]. The ionosphere and troposphere introduce further complexities that can impact positioning accuracy [2]. Furthermore, susceptibility to signal jamming or spoofing also poses challenges: GPS signal is very vulnerable to jamming because of its low operating power [3], and spoofing was already proved to be possible for unauthorized control of an autonomous Unmanned Aerial Vehicle (UAV) [4]. These inherent realities have prompted engineers and researchers to explore positioning techniques that could serve as alternatives to GPS.

The initial positioning methods during the Age of Discovery relied on accurate chronometers and celestial body observations. This approach is somewhat replicated in modern star trackers. Due to the limited daily time frame for celestial observations, these systems are primarily designed for application in space systems, such as planetary

rovers [5]. An interwar navigation innovation was the development of radio navigation systems, with hyperbolic navigation emerging as a primary representative. This approach is still being considered in some specific aviation applications [6]. Similarly to satellite navigation, radio navigation methods are also susceptible to jamming. Moreover, there is a trade-off between the range and accuracy of such systems, and their operation is affected by weather conditions. In contrast to the two methods mentioned above, a more modern navigation technique is vision-based navigation, also referred to as terrain-relative navigation. It became an object of interest alongside the development of computer technology, particularly with the evolution of computer vision methods. This technique is especially useful for the autonomous operation of aerial vehicles, navigating between two points designated by the operator from satellite images [7]. A more sophisticated application is the autonomous control of an aerial vehicle at low altitudes, which complements classical navigation methods when obstacle avoidance must be considered [8].

Several authors characterize their methodologies as extensions of standard navigation systems in the event of GPS signal loss. Their primary advantage over standard Inertial Navigation Systems (INS) lies in their ability to eliminate drift effectively [9]. However, they introduce an additional computational burden to the control unit. It could involve operating on geo-referenced satellite images [9] or performing a so-called memory building process, which entails storing a set of image

\* Corresponding author.

E-mail address: [ljank@ippt.pan.pl](mailto:ljank@ippt.pan.pl) (Ł. Jankowski).

<https://doi.org/10.1016/j.measurement.2024.114738>

Received 23 January 2024; Received in revised form 19 March 2024; Accepted 16 April 2024

Available online 20 April 2024

0263-2241/© 2024 The Author(s). Published by Elsevier Ltd. This is an open access article under the CC BY license (<http://creativecommons.org/licenses/by/4.0/>).

sequences and typically requires human operator involvement [10]. The estimation accuracy of such methods is also negatively affected by flight altitude because, at higher altitudes, the apparent displacement of ground objects is reduced. Additionally, they are unsuitable for very uniform landscapes, such as when flying over a sea or a desert. Another positioning strategy relies on gravity gradiometers, devices intended to measure the elements of the gravity gradient tensor [11]. The gravity gradiometers were initially developed for navigating submarines in the absence of alternative options (e.g., sonars) and later adopted for locating underground gas and oil deposits [12]. Scientific advancement in this field resulted in the development of passive (non-emanating) navigation systems that are robust to jamming and provide positioning capability over water [13]. Airborne applications as an aid to the INS, or in the absence of a GPS signal, are also one of the main fields of interest in this context [14–16], which includes searching for mineral deposits from aircraft [17,18]. Technological development has enabled attempts to measure the gravitational field from space [19]. The main disadvantage of such systems is the very cumbersome detection of man-made underwater objects [20]. There are also challenges associated with distinguishing between effects related to gravity and acceleration, as well as with extremely small acceleration levels affecting the correctness of the results.

The growing attention towards magnetic anomalies in the context of positioning and navigation systems finds its foundation in a range of inherent physical characteristics. First and foremost, magnetic signals exhibit global accessibility and are detectable in both outdoor and indoor settings with no restrictions related to daily time frames. Across the majority of terrains, magnetic anomalies sustain substantial diversity, facilitating their detection even within environments that might appear homogeneous to camera or radar-based systems, such as deserts, dense forests, or water reservoirs. Notably, the measurement of magnetic anomaly fields is achieved through passive instrumentation, devoid of self-emission signals. This feature becomes essential when integrating within complex, error-sensitive systems. It also needs to be emphasized that the efficient utilization of magnetic anomaly information requires addressing several challenging problems related to signal processing. In particular, it is essential to detect magnetic field disturbances that arise inherently, such as those associated with geomagnetic storms, and those related to the interference from neighboring electrical-powered devices.

To date, various methodologies have been developed for positioning based on the magnetic field and customized to the specific characteristics of the environment. In the context of indoor applications, localization is often combined with the mapping task, and this approach is known as Simultaneous Localization and Mapping (SLAM). It has gained popularity due to the increasing demand for autonomous mobile robots requiring precise navigation within indoor environments, where a referencing system, particularly GPS, is either unavailable or offers insufficient accuracy. Typically, SLAM methods incorporate radar and laser sensors [21], and they can be broadly categorized as filtering or smoothing [22]. Recent works also focus on utilizing cameras for this purpose, the so-called visual SLAM [23,24]. This approach can be implemented using classical stereovision systems or monocular ones [25]. Utilization of the ambient magnetic field for SLAM has gained special attention in recent years [26,27]. Localization algorithms in SLAM are commonly implemented using Kalman filters [28] or various versions of particle filters [29,30]. A sequential batch fusion algorithm for indoor magnetic map matching was proposed in [31], based on a combined use of magnetometers, gyroscopes, and wheel odometry. Indoor navigation with active beacons generating AC magnetic fields was considered in [32]. Extension of the techniques initially developed for SLAM to outdoor environments commonly results in using particle filter implementations for navigation purposes [33,34]. Iterative closest contour point algorithms are often used with swarm optimization approaches like ant colony optimization [35] or particle swarm optimization [36]. In airborne applications, estimating the Earth's magnetic anomaly field

is often used as a basis for developing navigation methods [37]. Using magnetic field measurements for aerial navigation requires proper calibration to isolate the influence of non-geological magnetic field sources. For this purpose, classical calibration methods, such as the linear calibration model, are successfully supplemented by machine learning methods [38].

In this paper, we leverage the magnetic field information and the Bayesian formalism to enhance the positioning accuracy initially estimated by a localization module. As in the case of inertial measurement units (IMU), the initial position estimate can be characterized by a significant drift, which can be partially corrected by exploiting the additional information provided by an onboard magnetometer. The proposed algorithm can be thus classified as a data-fusion method. In each time step, the initial expected position is shifted towards the suitable neighboring isoline of the magnetic field, and the localization variance is correspondingly decreased. The developed algorithm for position correction relies on simple closed-form formulas, facilitating real-time implementation. The method is tested and validated in laboratory conditions. Its effectiveness in correcting the position is examined along two trajectories that traverse distinct magnetic field characteristics. The presented analysis of the positioning accuracy includes the influence of magnetic field characteristics and the measurement error level of the magnetometer. Compared to previous approaches, the main contribution of this work is the development of a Bayesian data-fusion algorithm for real-time trajectory correction, based on magnetic field measurements, that has minimal computational costs and features a minimal number of arbitrary tunable parameters.

This paper is organized as follows: Section 2 introduces the architecture of the positioning system and outlines the necessary assumptions about its components. Subsequently, it describes the method used for magnetic field mapping and then presents and discusses the algorithm proposed for correcting the position. Section 3 describes the experimental setup and uses it to map the magnetic field. Section 4 applies and evaluates the proposed position correction method, discusses its accuracy, and compares it to a particle filter implementation. Finally, Section 5 offers concluding remarks.

## 2. Real-time positioning based on magnetic anomaly measurements

The primary limitation of state estimators commonly utilized for localization, such as Kalman or particle filters, is their incremental and iterative nature. This characteristic leads to high computational cost, hindering their application in real-time scenarios. Various modifications of these methods have been proposed to enhance their convergence rate [30]. Another challenge in adapting methods developed for indoor environments to outdoor settings is associated with the larger scale of the problem, leading to a significant increase in computational burden. Localization methods designed for indoor environments are occasionally tested outdoors; however, their applicability is generally limited to relatively small areas [39]. In this study, we aim to design a computationally efficient algorithm capable of an instantaneous localization correction, irrespective of the scale of the designated area.

### 2.1. System operation and objectives

The general scheme of the proposed system is depicted in Fig. 1. Suppose the reference positioning system (in particular GPS) is available. In that case, it provides the absolute position of the object to be utilized by both the navigation system and the magnetic anomaly map module, which creates and updates the magnetic anomaly map. However, if the reference positioning system is unavailable, the primary information about object position is obtained from a built-in localization module such as IMU. This module provides an estimate of the current position based on differential measurements. Given the magnetic anomaly map and a magnetometer, magnetic corrections can be

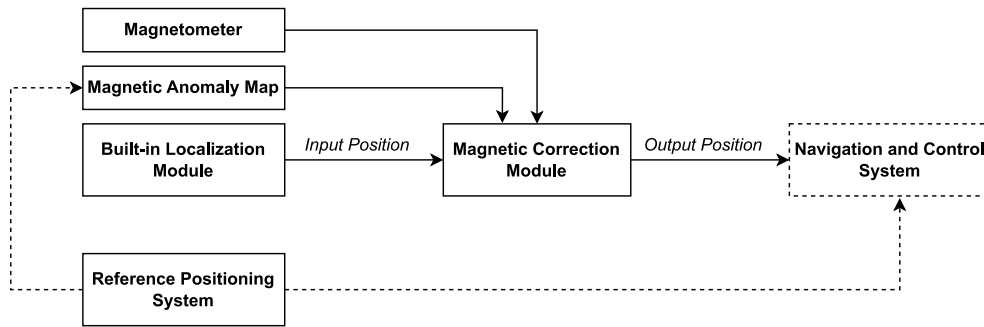


Fig. 1. General scheme of the proposed localization system based on magnetic corrections.

additionally computed and applied to obtain a corrected, more precise position. Therefore, when information from the reference positioning system is lost or identified as unreliable, the magnetic correction module can be activated, in addition to the built-in localization module, to provide enhanced localization information.

The data recorded by the built-in localization module exhibit noise, resulting in cumulative errors that increase over time. Conversely, magnetic field readings do not exhibit drift but are susceptible to random external and internal disturbances and the effects of device magnetization. This work focuses on achieving an efficient trajectory correction procedure suitable for real-time operation. The mapping subsystem is thus required to provide input data that is sufficiently accurate for this task. This is stated here in the form of the following four general assumptions:

- A1. Trajectory drift introduced by the built-in localization module is sufficiently limited.
- A2. Magnetometer sensitivity and accuracy of the reference positioning system are sufficient to obtain magnetic field maps of adequate precision.
- A3. Spatial variability of the magnetic field allows for local linearization and Gaussian representation of the involved probability distributions.
- A4. The magnetic anomaly field within the considered area can be considered stationary in time.

These assumptions focus the work on the proposed correction algorithm. In particular, A1 ensures that the input trajectory provided by the built-in positioning system, even if inaccurate, is still relevant to the actual trajectory. Abandoning A1 would shift the focus from correcting an inaccurate trajectory to full positioning based solely on magnetic measurements. A2 to A4 limit the uncertainty of the magnetic anomaly map to the level that can be accounted for using a single measurement variance parameter ( $\sigma_M^2$  in Table 1). More significant variability of the field needs to be addressed separately, for example by incorporating dedicated SLAM techniques. This is a challenging problem but beyond the immediate scope of this work. Based on the above assumptions, important objectives of this work are related to efficiency:

- O1. *Minimal computational cost* of the proposed algorithm. It avoids cumulative delays and enables real-time operation instantaneously after the loss of the reference positioning system.
- O2. *Minimal number of tunable parameters*. Typical positioning methods, including those based on particle filtering, tend to have many tunable parameters that must be individually adjusted in a time-consuming procedure. The algorithm proposed here has only one adjustable parameter, whose value is selected in reference to a physical quantity: the variance of magnetic field measurements.

This study focuses on two-dimensional localization, limited to longitude and latitude, without considering altitude. Extending the framework to perform three-dimensional positioning is straightforward but

requires altitude-dependent magnetic field maps. In majority of the cases, this altitude-dependency can be effectively established by employing the International Geomagnetic Reference Field (IGRF) model [40]. The remaining elements of the positioning correction framework would be preserved in the transition to the three-dimensional setting.

## 2.2. Magnetic anomaly mapping

A number of approaches have been developed and implemented in positioning and navigation systems to build accurate magnetic field maps. In [41], magnetometer measurements were collected in a grid and then linearly interpolated to approximate the magnetic field distribution. The method was successfully validated for localization using a particle filter incorporating data acquired from a magnetometer and accelerometer. In [42], the spatial binning method was adopted to represent the magnetic field intensity, subsequently utilized in the SLAM approach to localize pedestrians equipped with IMU. Here, the magnetic field is modeled using Gaussian regression [43,44], and this choice is motivated by two factors. Firstly, Gaussian regression with an exponential kernel has demonstrated its ability to reconstruct typical shapes of magnetic anomalies [29], even with limited measurement data. Secondly, the positioning algorithm leverages the smooth functions reproduced by Gaussian regression when computing the magnetic field gradient (see Section 2.3.3).

Assume that we have at disposal a set of magnetic field measurements  $M^1(\bar{\mathbf{x}}^1), \dots, M^m(\bar{\mathbf{x}}^m)$  acquired with some Gaussian noise  $\epsilon \sim \mathcal{N}(0, \sigma_M^2)$  at the respective locations  $\bar{\mathbf{x}}^1, \dots, \bar{\mathbf{x}}^m \in X \subset \mathbb{R}^2$ . Using the assumption that  $M^1(\bar{\mathbf{x}}^1), \dots, M^m(\bar{\mathbf{x}}^m)$  are related to a Gaussian process  $\mathcal{M}$ , a continuous interpolating function  $M : X \rightarrow \mathbb{R}$  can be established as the mean of the posterior distribution,  $M(\mathbf{x}) = \mathbb{E}[\mathcal{M}(\mathbf{x}) | M^1(\bar{\mathbf{x}}^1), \dots, M^m(\bar{\mathbf{x}}^m)]$ . Using the Bayes rule [45] it follows that the posterior distribution

$$\mathcal{M}(\mathbf{x}) | M^1(\bar{\mathbf{x}}^1), \dots, M^m(\bar{\mathbf{x}}^m) \sim \mathcal{N}(\mu_{\mathcal{M}}, \sigma_{\mathcal{M}}^2), \quad (1)$$

where the mean  $\mu_{\mathcal{M}}$  is a function of  $\mathbf{x} \in X \subset \mathbb{R}^2$  given by:

$$\mu_{\mathcal{M}}(\mathbf{x}) = [\kappa(\mathbf{x}, \bar{\mathbf{x}}^1), \dots, \kappa(\mathbf{x}, \bar{\mathbf{x}}^m)]^T (\mathbf{C} + \sigma_M \mathbf{I})^{-1} [M^1(\bar{\mathbf{x}}^1), \dots, M^m(\bar{\mathbf{x}}^m)]. \quad (2)$$

In (2),  $\kappa$  stands for the covariance kernel function which is assumed to be represented by the Gaussian function,

$$\kappa(\mathbf{x}, \bar{\mathbf{x}}^i) = \sigma^2 \exp\left(-\frac{\|\mathbf{x} - \bar{\mathbf{x}}^i\|^2}{2l^2}\right), \quad i = 1, \dots, m, \quad (3)$$

and parameterized with the signal variance  $\sigma^2$  and the length scale  $l$ . Further,  $\mathbf{I}$  in (2) is the identity matrix, and the covariance matrix  $\mathbf{C}$  is computed using:

$$\mathbf{C} = [c_{i,j}]_{m \times m}, \quad c_{i,j} = \kappa(\bar{\mathbf{x}}^i, \bar{\mathbf{x}}^j). \quad (4)$$

Therefore, for every location  $\mathbf{x} \in X \subset \mathbb{R}^2$  the function  $M$  can be represented by  $\mu_{\mathcal{M}}(\mathbf{x})$ :

$$M(\mathbf{x}) = [\kappa(\mathbf{x}, \bar{\mathbf{x}}^1), \dots, \kappa(\mathbf{x}, \bar{\mathbf{x}}^m)]^T (\mathbf{C} + \sigma_M \mathbf{I})^{-1} [M^1(\bar{\mathbf{x}}^1), \dots, M^m(\bar{\mathbf{x}}^m)]. \quad (5)$$

**Table 1**  
Localization-related nomenclature.

$\mathbf{x}, \mathbf{y} \in \mathbb{R}^2$	locations in a 2D space (deterministic two-element vectors)
$M(\mathbf{x})$	magnetic field map at location $\mathbf{x}$ (deterministic number)
$f_A(\mathbf{x})$	probability density function of the random variable $\mathbf{A}$
$\mathbf{Z}_t$	location determined at time $t$ by the magnetic localization system (2D random variable)
$\mathbf{X}_t$	location reported at time $t$ by the built-in localization system (2D random variable)
$\Delta\mathbf{X}_t = \mathbf{X}_t - \mathbf{X}_{t-1}$	location update reported at time $t$ by the built-in localization system (2D random variable)
$\mathbf{Y}_t = \mathbf{Z}_{t-1} + \Delta\mathbf{X}_t$	location at time $t$ obtained by shifting $\mathbf{Z}_{t-1}$ by $\Delta\mathbf{X}_t$ (2D random variable)
$\bar{\mathbf{Z}}_t = \mathbf{X}_t  _{\mathbf{Y}_t = \mathbf{x}}$	location obtained by fusing $\mathbf{X}_t$ and $\mathbf{Y}_t$ (2D random variable)
$M_t = M(\bar{\mathbf{Z}}_t) + \epsilon$	measurement of the magnetometer at location $\bar{\mathbf{Z}}_t$ (1D random variable)
$\epsilon \sim \mathcal{N}(0, \sigma_M^2)$	magnetic field measurement error (1D random variable)

All location-related random variables are assumed to be normally distributed.

The hyperparameters  $\sigma$  and  $l$  in (3) are selected by maximizing the log marginal likelihood:

$$J(\sigma, l) = -\frac{1}{2} [M^1(\bar{\mathbf{x}}^1), \dots, M^m(\bar{\mathbf{x}}^m)]^T (C + \sigma_M \mathbf{I})^{-1} [M^1(\bar{\mathbf{x}}^1), \dots, M^m(\bar{\mathbf{x}}^m)] - \frac{1}{2} \log(\det(C + \sigma_M \mathbf{I})) - \frac{m}{2} \log(2\pi). \quad (6)$$

From (6), it follows that the optimal pair of hyperparameters  $(\sigma^*, l^*)$  satisfies the following necessary optimality condition:

$$\frac{\partial J}{\partial \sigma}(\sigma^*, l^*) = 0, \quad \frac{\partial J}{\partial l}(\sigma^*, l^*) = 0. \quad (7)$$

To compute  $(\sigma^*, l^*)$ , the gradient descent method is employed.

### 2.3. Real-time accurate localization using magnetic corrections

#### 2.3.1. Data sources for localization

If neither the reference positioning (such as GPS) nor the magnetic localization systems are available/activated, the only available source of information on the current location is the built-in localization system (for example, an inertial localization system). In each time step  $t$ , it reports the location  $\mathbf{X}_t$  and its update from the previous time step, denoted by  $\Delta\mathbf{X}_t = \mathbf{X}_t - \mathbf{X}_{t-1}$ . Both  $\mathbf{X}_t$  and  $\Delta\mathbf{X}_t$  are modeled as 2D random variables, and as with all other location-related random variables, they are assumed to be normally distributed in the following. For clarity, the localization-related nomenclature is presented in Table 1.

If available and activated, the magnetic localization system provides the corrected location  $\mathbf{Z}_t$  in each time step  $t$ . This location is computed by fusing information on location obtained from as many as three information sources:

1. location  $\mathbf{X}_t$  reported in each time step by the built-in localization system,
2. location  $\mathbf{Y}_t$ , which is obtained by shifting the location  $\mathbf{Z}_{t-1}$  (determined in the previous time step) by the update  $\Delta\mathbf{X}_t$  (provided by the built-in localization system),  $\mathbf{Y}_t = \mathbf{Z}_{t-1} + \Delta\mathbf{X}_t$ ,
3. magnetic field measurement  $M_t$  provided by the magnetometer.

#### 2.3.2. Two-step data fusion procedure

The information obtained from the three data sources listed above is fused into a single a posteriori location  $\mathbf{Z}_t$  using the Bayesian formalism. This process is performed in two steps:

**Step 1.** The random variables  $\mathbf{X}_t$  and  $\mathbf{Y}_t$  are treated as the a priori information about the current location. These two variables are fused into a single random variable  $\bar{\mathbf{Z}}_t$ . The natural postulate that  $\mathbf{X}_t = \mathbf{Y}_t$  plays the role of the evidence.

**Step 2.** The fused location  $\bar{\mathbf{Z}}_t$  is treated as the a priori location and updated into the final location  $\mathbf{Z}_t$ . The evidence is the specific value  $M_t = m_t$  provided by the magnetometer as the result of the (noisy) measurement of the magnetic field intensity.

*Step 1.* In Step 1, the input random variables are assumed to be normally distributed with the following means and covariance matrices:

$$\mathbf{Z}_{t-1} \sim \mathcal{N}(\boldsymbol{\mu}_{\mathbf{Z}_{t-1}}, \boldsymbol{\Sigma}_{\mathbf{Z}_{t-1}}), \quad (8)$$

$$\mathbf{X}_t \sim \mathcal{N}(\boldsymbol{\mu}_{\mathbf{X}_t}, \boldsymbol{\Sigma}_{\mathbf{X}_t}), \quad (9)$$

$$\Delta\mathbf{X}_t \sim \mathcal{N}(\boldsymbol{\mu}_{\Delta\mathbf{X}_t}, \boldsymbol{\Sigma}_{\Delta\mathbf{X}_t}). \quad (10)$$

The random variables  $\mathbf{Z}_{t-1}$  and  $\Delta\mathbf{X}_t$  are treated as independent, which enables a straightforward calculation of the shifted location  $\mathbf{Y}_t$ :

$$\mathbf{Y}_t = \mathbf{Z}_{t-1} + \Delta\mathbf{X}_t \sim \mathcal{N}(\boldsymbol{\mu}_{\mathbf{Y}_t}, \boldsymbol{\Sigma}_{\mathbf{Y}_t}), \quad (11)$$

where  $\boldsymbol{\mu}_{\mathbf{Y}_t} = \boldsymbol{\mu}_{\mathbf{Z}_{t-1}} + \boldsymbol{\mu}_{\Delta\mathbf{X}_t}$  and  $\boldsymbol{\Sigma}_{\mathbf{Y}_t} = \boldsymbol{\Sigma}_{\mathbf{Z}_{t-1}} + \boldsymbol{\Sigma}_{\Delta\mathbf{X}_t}$ . The variables  $\mathbf{X}_t$  and  $\mathbf{Y}_t$  are treated as the a priori information on the location in time step  $t$ . For the derivation simplicity, they are assumed to be independent, so that their joint probability density function is given by:

$$f_{\mathbf{X}_t, \mathbf{Y}_t}(\mathbf{x}, \mathbf{y}) = f_{\mathbf{X}_t}(\mathbf{x}) f_{\mathbf{Y}_t}(\mathbf{y}) \sim \exp\left(-\frac{1}{2}(\mathbf{x} - \boldsymbol{\mu}_{\mathbf{X}_t})^T \boldsymbol{\Sigma}_{\mathbf{X}_t}^{-1}(\mathbf{x} - \boldsymbol{\mu}_{\mathbf{X}_t}) - \frac{1}{2}(\mathbf{y} - \boldsymbol{\mu}_{\mathbf{Y}_t})^T \boldsymbol{\Sigma}_{\mathbf{Y}_t}^{-1}(\mathbf{y} - \boldsymbol{\mu}_{\mathbf{Y}_t})\right). \quad (12)$$

Given the natural postulate that  $\mathbf{X}_t = \mathbf{Y}_t$ , which is treated as the evidence, the probability density function of the a posteriori location  $\bar{\mathbf{Z}}_t$  equals

$$f_{\bar{\mathbf{Z}}_t}(\mathbf{x}) = f_{\mathbf{X}_t, \mathbf{Y}_t | \mathbf{X}_t = \mathbf{Y}_t}(\mathbf{x}, \mathbf{x}) \sim f_{\mathbf{X}_t}(\mathbf{x}) f_{\mathbf{Y}_t}(\mathbf{x}) \sim \exp\left(-\frac{1}{2}(\mathbf{x} - \boldsymbol{\mu}_{\mathbf{X}_t})^T \boldsymbol{\Sigma}_{\mathbf{X}_t}^{-1}(\mathbf{x} - \boldsymbol{\mu}_{\mathbf{X}_t}) - \frac{1}{2}(\mathbf{x} - \boldsymbol{\mu}_{\mathbf{Y}_t})^T \boldsymbol{\Sigma}_{\mathbf{Y}_t}^{-1}(\mathbf{x} - \boldsymbol{\mu}_{\mathbf{Y}_t})\right) \sim \exp\left(-\frac{1}{2}(\mathbf{x} - \boldsymbol{\mu}_{\bar{\mathbf{Z}}_t})^T \boldsymbol{\Sigma}_{\bar{\mathbf{Z}}_t}^{-1}(\mathbf{x} - \boldsymbol{\mu}_{\bar{\mathbf{Z}}_t})\right). \quad (13)$$

Consequently,  $\bar{\mathbf{Z}}_t$  is normally distributed,

$$\bar{\mathbf{Z}}_t \sim \mathcal{N}(\boldsymbol{\mu}_{\bar{\mathbf{Z}}_t}, \boldsymbol{\Sigma}_{\bar{\mathbf{Z}}_t}), \quad (14)$$

and

$$\boldsymbol{\Sigma}_{\bar{\mathbf{Z}}_t} = \left(\boldsymbol{\Sigma}_{\mathbf{X}_t}^{-1} + \boldsymbol{\Sigma}_{\mathbf{Y}_t}^{-1}\right)^{-1}, \quad (15)$$

$$\boldsymbol{\mu}_{\bar{\mathbf{Z}}_t} = \boldsymbol{\Sigma}_{\bar{\mathbf{Z}}_t} \left(\boldsymbol{\Sigma}_{\mathbf{X}_t}^{-1} \boldsymbol{\mu}_{\mathbf{X}_t} + \boldsymbol{\Sigma}_{\mathbf{Y}_t}^{-1} \boldsymbol{\mu}_{\mathbf{Y}_t}\right). \quad (16)$$

*Step 2.* In Step 2, the magnetic field measurement error  $\epsilon \sim \mathcal{N}(0, \sigma_M^2)$  and the location  $\bar{\mathbf{Z}}_t$  are assumed to be independent. Given that  $M_t = M(\bar{\mathbf{Z}}_t) + \epsilon$ , see Table 1, this means that the probability density function of the joint distribution of  $\bar{\mathbf{Z}}_t$  and  $M_t$  is given by:

$$f_{\bar{\mathbf{Z}}_t, M_t}(\mathbf{x}, m) = f_{\bar{\mathbf{Z}}_t}(\mathbf{x}) f_{M_t | \bar{\mathbf{Z}}_t = \mathbf{x}}(m) \sim \exp\left(-\frac{1}{2}(\mathbf{x} - \boldsymbol{\mu}_{\bar{\mathbf{Z}}_t})^T \boldsymbol{\Sigma}_{\bar{\mathbf{Z}}_t}^{-1}(\mathbf{x} - \boldsymbol{\mu}_{\bar{\mathbf{Z}}_t}) - \frac{1}{2} \frac{(m - M(\mathbf{x}))^2}{\sigma_M^2}\right). \quad (17)$$

Given the specific outcome  $M_t = m_t$  of the magnetic field measurement, the a posteriori distribution of the current location is given as

$$\mathbf{Z}_t = \bar{\mathbf{Z}}_t | (M_t = m_t), \quad (18)$$

and its probability density function satisfies:

$$f_{\mathbf{Z}_t}(\mathbf{x}) = f_{\bar{\mathbf{Z}}_t | M_t = m_t}(\mathbf{x}) \sim f_{\bar{\mathbf{Z}}_t, M_t}(\mathbf{x}, m_t). \quad (19)$$

**Table 2**  
Bayesian data fusion procedure for magnetic correction of location.

Initialization:	$\mathbf{Z}_0 := \mathbf{X}_0, \quad t := 1$
Time step $t$ :	
Input:	<p>means and covariance matrices of the location-related variables</p> <p><math>\mathbf{Z}_{t-1} \sim \mathcal{N}(\boldsymbol{\mu}_{\mathbf{Z}_{t-1}}, \boldsymbol{\Sigma}_{\mathbf{Z}_{t-1}})</math> (from the previous step)</p> <p><math>\mathbf{X}_t \sim \mathcal{N}(\boldsymbol{\mu}_{\mathbf{X}_t}, \boldsymbol{\Sigma}_{\mathbf{X}_t})</math> (from the built-in localization system)</p> <p><math>\Delta \mathbf{X}_t \sim \mathcal{N}(\boldsymbol{\mu}_{\Delta \mathbf{X}_t}, \boldsymbol{\Sigma}_{\Delta \mathbf{X}_t})</math> (from the built-in localization system)</p> <p>variance of the magnetic field measurement error</p> <p><math>\sigma_M^2</math></p> <p>result of the magnetic field measurement (from magnetometer)</p> <p><math>m_t</math></p>
Computations:	<p>(1°) mean and covariance matrix of the location <math>\mathbf{Y}_t = \mathbf{Z}_{t-1} + \Delta \mathbf{X}_t</math></p> <p><math>\boldsymbol{\mu}_{\mathbf{Y}_t} = \boldsymbol{\mu}_{\mathbf{Z}_{t-1}} + \boldsymbol{\mu}_{\Delta \mathbf{X}_t}</math></p> <p><math>\boldsymbol{\Sigma}_{\mathbf{Y}_t} = \boldsymbol{\Sigma}_{\mathbf{Z}_{t-1}} + \boldsymbol{\Sigma}_{\Delta \mathbf{X}_t}</math></p> <p>(2°) mean and covariance matrix of the fused <math>\tilde{\mathbf{Z}}_t = \mathbf{X}_t   (\mathbf{X}_t = \mathbf{Y}_t)</math></p> <p><math>\boldsymbol{\Sigma}_{\tilde{\mathbf{Z}}_t} = (\boldsymbol{\Sigma}_{\mathbf{X}_t}^{-1} + \boldsymbol{\Sigma}_{\mathbf{Y}_t}^{-1})^{-1}</math></p> <p><math>\boldsymbol{\mu}_{\tilde{\mathbf{Z}}_t} = \boldsymbol{\Sigma}_{\tilde{\mathbf{Z}}_t} (\boldsymbol{\Sigma}_{\mathbf{X}_t}^{-1} \boldsymbol{\mu}_{\mathbf{X}_t} + \boldsymbol{\Sigma}_{\mathbf{Y}_t}^{-1} \boldsymbol{\mu}_{\mathbf{Y}_t})</math></p> <p>(3°) mean and covariance matrix of <math>\mathbf{Z}_t = \tilde{\mathbf{Z}}_t   (M_t = m_t)</math></p> <p><math>\boldsymbol{\Sigma}_{\mathbf{Z}_t} = \left( \boldsymbol{\Sigma}_{\tilde{\mathbf{Z}}_t}^{-1} + \frac{\nabla M(\boldsymbol{\mu}_{\tilde{\mathbf{Z}}_t}) (\nabla M(\boldsymbol{\mu}_{\tilde{\mathbf{Z}}_t}))^T}{\sigma_M^2} \right)^{-1}</math></p> <p><math>\boldsymbol{\mu}_{\mathbf{Z}_t} = \boldsymbol{\mu}_{\tilde{\mathbf{Z}}_t} + \frac{m_t - M(\boldsymbol{\mu}_{\tilde{\mathbf{Z}}_t})}{\sigma_M^2} \boldsymbol{\Sigma}_{\tilde{\mathbf{Z}}_t} \nabla M(\boldsymbol{\mu}_{\tilde{\mathbf{Z}}_t})</math></p>
Time step update:	$t := t + 1$
Output:	means and covariance matrices of the corrected locations
	$\boldsymbol{\mu}_{\mathbf{Z}_t}, \boldsymbol{\Sigma}_{\mathbf{Z}_t}$

The magnetic map  $M(\mathbf{x})$  is locally linearized around  $\boldsymbol{\mu}_{\tilde{\mathbf{Z}}_t}$ ,

$$M(\mathbf{x}) \approx M(\boldsymbol{\mu}_{\tilde{\mathbf{Z}}_t}) + (\mathbf{x} - \boldsymbol{\mu}_{\tilde{\mathbf{Z}}_t})^T \nabla M(\boldsymbol{\mu}_{\tilde{\mathbf{Z}}_t}), \quad (20)$$

and the linearization is substituted into the joint distribution (17). Given (19), this finally yields the following a posteriori probability density function of  $\mathbf{Z}_t$ :

$$f_{\mathbf{Z}_t}(\mathbf{x}) \sim \exp\left(-\frac{1}{2}(\mathbf{x} - \boldsymbol{\mu}_{\mathbf{Z}_t})^T \boldsymbol{\Sigma}_{\mathbf{Z}_t}^{-1} (\mathbf{x} - \boldsymbol{\mu}_{\mathbf{Z}_t})\right), \quad (21)$$

where

$$\boldsymbol{\Sigma}_{\mathbf{Z}_t} = \left( \boldsymbol{\Sigma}_{\tilde{\mathbf{Z}}_t}^{-1} + \frac{\nabla M(\boldsymbol{\mu}_{\tilde{\mathbf{Z}}_t}) (\nabla M(\boldsymbol{\mu}_{\tilde{\mathbf{Z}}_t}))^T}{\sigma_M^2} \right)^{-1}, \quad (22)$$

$$\boldsymbol{\mu}_{\mathbf{Z}_t} = \boldsymbol{\mu}_{\tilde{\mathbf{Z}}_t} + \frac{m_t - M(\boldsymbol{\mu}_{\tilde{\mathbf{Z}}_t})}{\sigma_M^2} \boldsymbol{\Sigma}_{\tilde{\mathbf{Z}}_t} \nabla M(\boldsymbol{\mu}_{\tilde{\mathbf{Z}}_t}), \quad (23)$$

and  $\boldsymbol{\Sigma}_{\mathbf{Z}_t}$  and  $\boldsymbol{\mu}_{\mathbf{Z}_t}$  are defined as in (16). Consequently,  $\mathbf{Z}_t$  is normally distributed:

$$\mathbf{Z}_t \sim \mathcal{N}(\boldsymbol{\mu}_{\mathbf{Z}_t}, \boldsymbol{\Sigma}_{\mathbf{Z}_t}). \quad (24)$$

The standard deviation  $\sigma_M$  quantifies the error  $\epsilon \sim \mathcal{N}(0, \sigma_M^2)$  of the magnetic field measurement. However, an additional error is entailed in the linearization (20). If its dependence on the location  $\tilde{\mathbf{Z}}_t$  is ignored (or averaged out), it can be included in the measurement error  $\epsilon$  and accounted for by increasing its standard deviation  $\sigma_M$ . Similarly,  $\sigma_M$  may also be increased to account for the inaccuracies of the magnetic map  $M$ . Consequently,  $\sigma_M$  is the sole tunable parameter of the proposed procedure, as stated in the objective O2 in Section 2.1.

The entire two-step Bayesian data fusion procedure is summarized in Table 2. Numerically, it involves only straightforward sums, inversions, and products of  $2 \times 2$  matrices and 2-element vectors. These negligible numerical costs make the procedure suitable for real-time operation and agree with the objective O1 listed in Section 2.1.

### 2.3.3. Reduction of location uncertainty

The magnetic field is measured at each time step. According to (22) and (23), the proposed Bayesian procedure shifts the expected

value of the location and increases its accuracy (decreasing the variance/uncertainty) in the direction associated with the gradient  $\nabla M(\boldsymbol{\mu}_{\tilde{\mathbf{Z}}_t})$  of the magnetic field. As seen in (22), location accuracy increases together with the gradient norm and together with the accuracy of the magnetometer measurements  $\sigma_M^{-1}$ .

The reduction of variance can be illustrated as shown in Fig. 2. The background contour map represents the magnetic field intensity, as measured and mapped on the lab test stand (Section 3.3), with explicitly marked isolines. The variance reduction is demonstrated for 16 points distributed in a regular  $4 \times 4$  grid. The black circles represent the initial location uncertainty (prior to correction) and correspond to the probability density function isolines containing 50% of the probability mass. The red and green ellipses contain the corresponding 50% probability mass after the location variance is corrected by (22). Two levels of standard deviation for the magnetic field measurement error are considered:  $\sigma_M = 10\%$  (red lines) and  $\sigma_M = 1\%$  (green lines), expressed relative to the full magnetic field range on the map. Significant reduction of variance along the gradient can be observed. As expected, the variance along magnetic field isolines remains unaffected by the correction, so that location uncertainty is not improved in the direction perpendicular to the gradient.

## 3. Experimental stand and instrumentation

### 3.1. Laboratory stand

A laboratory setup was designed to verify and demonstrate the effectiveness of the developed method. Fig. 3 presents an overview of the experimental stand and its essential components. The system consists of a base plate, a subsystem for generating the magnetic field, a lighting system, a mobile measurement platform, and a vision system. The vision system tracks the movement of the mobile platform and records the reference trajectory. The base plate is made from chipboard covered with a laminate layer with a low coefficient of friction to eliminate self-excited vibrations of the mobile measuring platform. The base plate is 1600 mm by 2000 mm in dimension and is supported by six steel legs. Under the base plate, two sets of ferromagnetic magnets are mounted (see Fig. 4). They are connected to the plate

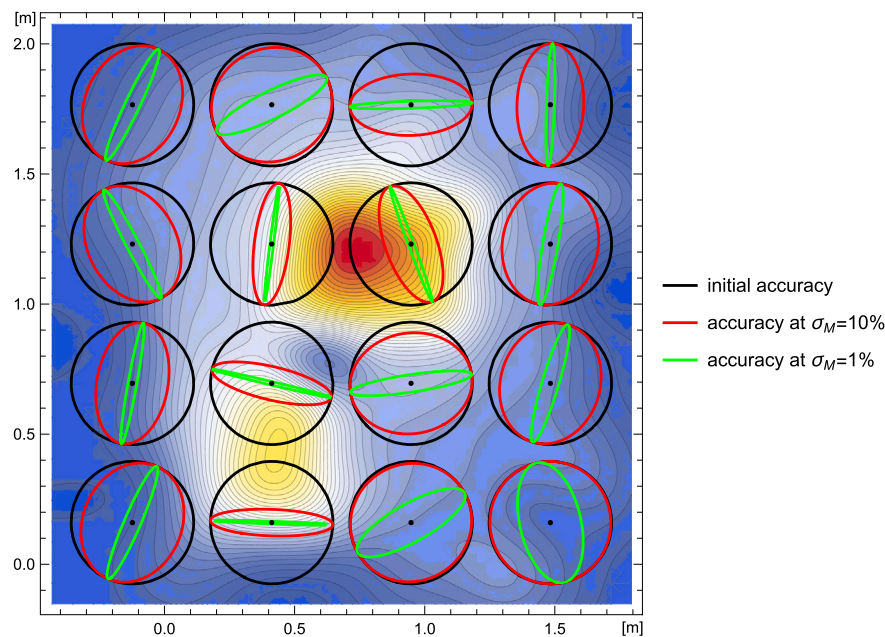


Fig. 2. Reduction of variance (location uncertainty) due to magnetometric measurements. The ellipses contain 50% of the location probability mass before the correction (black) and after the correction by (22) (red and green).

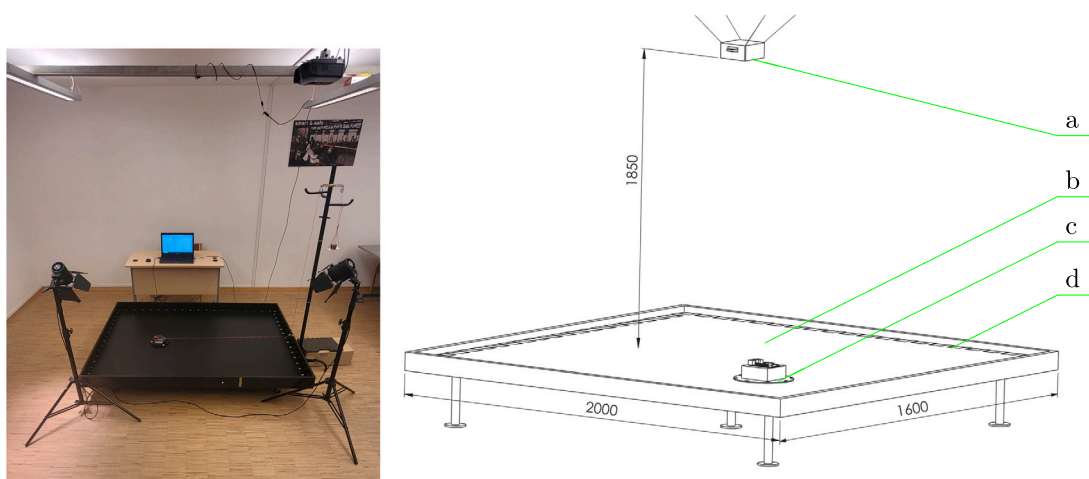


Fig. 3. Experimental test stand: a – camera (Creative Live Cam), b – base plate, c – mobile measurement platform with Xsens MTi-630, d – fluorescent markers.

bottom surface by links of adjustable length, which enable changing the intensity of the magnetic field on the test rig. With the increasing length of the links, the intensity of the magnetic field measured on the surface of the base plate decreases. Each set of magnets generates its own magnetic field, which differs from the other in terms of shape and value. As a result, different magnetic field distributions can be easily obtained, and system operations can be tested under different environmental conditions. The specific arrangement of ferromagnetic magnets depicted in Fig. 4 was selected to obtain a magnetic field whose general characteristics resemble those of typical anomalies of the Earth’s magnetic field. The field is shaped to obtain different gradients along the trajectories of the moving platform. Additionally, a part of the field on the test stand was designed to be relatively flat and have a minimal gradient.

### 3.2. Measurement systems and data processing

The source of reference trajectory, required for assessing the effectiveness of the proposed localization algorithm, is the vision system

discussed in this section. The vision system tracks the movement of the mobile platform, equipped with an inertial measurement unit (IMU), a magnetometer, and a magnetic field map. These components of the localization system are introduced in consecutive subsections.

#### 3.2.1. Vision system

The vision measurement system is employed to obtain the positions of the markers and the reference location of the mobile platform in a two-dimensional (2D) Cartesian coordinate system associated with the base plate. The system utilizes a camera with an image resolution of  $1920 \times 1080$  pixels, placed at a distance of 1850 mm from the surface of the base plate (see Fig. 3). Such placement enables the camera to track the mobile platform’s displacement with a resolution accuracy of  $\pm 1$  mm. The system records video footage of the mobile platform at a rate of 30 frames per second, which enables continuous measurement of the movement trajectory at speeds up to 3 m/s. To enhance image contrast for subsequent vision processing, spotlights from two lamps are directed at the photo-luminescent markers mounted on the mobile platform and around the base plate.



Fig. 4. System for creating magnetic field on the test stand.

A series of image processing steps is used to process the images captured by the camera and obtain the precise localization of the markers in the image plane. Initially, each video frame is converted to the HSV (hue, saturation, value) color space model. This model resembles human eye perception and is more suitable than RGB for color-based object tracking and image processing [46]. A MATLAB code, developed using the Threshold Color Image<sup>1</sup> algorithm, is then used to identify the thresholds for the HSV color components of the photo-luminescent markers. The resulting filtering masks isolate the image pixels corresponding to the markers. Subsequently, the color matching method [47] is employed to extract and process the respective pixel clusters. The coordinates of their geometric centers of gravity are interpreted as the location of the markers.

The IMU housing is elevated above the plane of the base plate, as shown in Fig. 5. To mitigate errors related to the parallax effect, three photo-luminescent markers are placed on the base of the mobile platform, marked as “c” in Fig. 5. The geometric center of these markers is determined as the location of the magnetometer integrated with the center of the IMU housing.

The camera’s optics introduce geometric distortions to the recorded images, which are corrected by recalculating the relative positions of the pixels in the image matrix using the transformation procedures described in [48–50]. Radial and tangential distortion coefficients, determined through heuristic calibration [51], are used to adjust the horizontal and vertical positions of pixels [49]. This process is repeated for each frame recorded by the camera of the vision measurement system. Prior to each measurement, the vision measurement system self-adapts by automatic scaling, recording the intensity of markers’ reflection, and compensating for the perspective effect and optical edge distortion.

### 3.2.2. Inertial measurement unit

The vision system measures the reference real trajectory of the mobile platform. This trajectory is synchronized in the time domain with the data recorded by the mobile measurement platform, providing a crucial second set of measurements for the localization module. The platform is based on a Xsens MTi 600 Inertial Measurement Unit (IMU), as depicted in Fig. 5, which includes an MTi-630 integrated circuit. This circuit registers parameters such as acceleration ( $\pm 100 \text{ m/s}^2$ , 2000 Hz), rotation angles ( $\pm 2000 \text{ deg/s}$ , 400 Hz), and magnetic field intensity ( $\pm 8 \text{ G}$ , 400 Hz).

The measurement noise of the magnetometer, quantified using its root mean square (rms) value, was estimated to be at the relatively low level of 0.002 G. In terms of the full range of the magnetic field intensity in the considered domain, which was approximately

8.7 G (see Section 3.3), this rms measurement error amounted to only 0.23%. To account for real scenarios, where the actual error can be significantly larger due to various additional disturbances, the noise rms in subsequent computations was conservatively assumed to be 1% of the field full range.

### 3.3. Mapping of magnetic anomaly field

The map of the magnetic field, generated on the experimental stand, was obtained using the method described in Section 2.2, with  $m = 1000$  measurements collected as shown in Fig. 6 (left). The optimal hyperparameters, satisfying condition (7), were determined to be  $\sigma^* = 8.6 \cdot 10^{-4}$  and  $l^* = 2.38 \cdot 10^{-1}$ . The resulting magnetic field distribution is depicted in Fig. 6 (right). The illustrated domain corresponds to the base plate. For numerical purposes of trajectory simulation, the field can be extrapolated beyond the boundary of the plate.

## 4. Experimental demonstration

### 4.1. Reference and IMU-based trajectories

The mobile platform, with the IMU onboard, completed a bow-shaped loop trajectory (trajectory A), as shown in Fig. 7 (left). The actual reference trajectory, registered using the vision system, is depicted in black, while the trajectory reported by the IMU is in red. The background represents the magnetic field intensity. The proposed correction procedure was applied to this original trajectory A and, for additional verification, to the same trajectory subjected to a numerical vertical flip (trajectory B), shown in Fig. 7 (right).

Fig. 7 confirms the limited accuracy of the built-in inertial localization system. The time evolution of the localization error is plotted in Fig. 8 (left) using the black line. This depicted error represents the distance between the reference position reported by the vision system and the position reported by the IMU-based localization system. The error increases from 0 cm at the start of the motion (where the initial position is known) up to 41.2 cm at the end. The mean value of the error is 11.9 cm.

### 4.2. Trajectory correction based on magnetic field measurements

The correction procedure proposed in Section 2.3.2 was applied to the two trajectories depicted in Fig. 7. Magnetic field measurements were read from the map at the actual position of the mobile platform reported by the vision system. Measurement noise was simulated by adding uncorrelated Gaussian noise at the level of 1%, as discussed at the end of Section 3.2.2. The parameter  $\sigma_M$ , used in the correction procedure (Table 2), was additionally increased by 5% to account for the magnetic map inaccuracies and the error related to the local linearization (20) of the magnetic field, as discussed at the end of

<sup>1</sup> <https://www.mathworks.com/help/images/ref/colorthresholder-app.html>

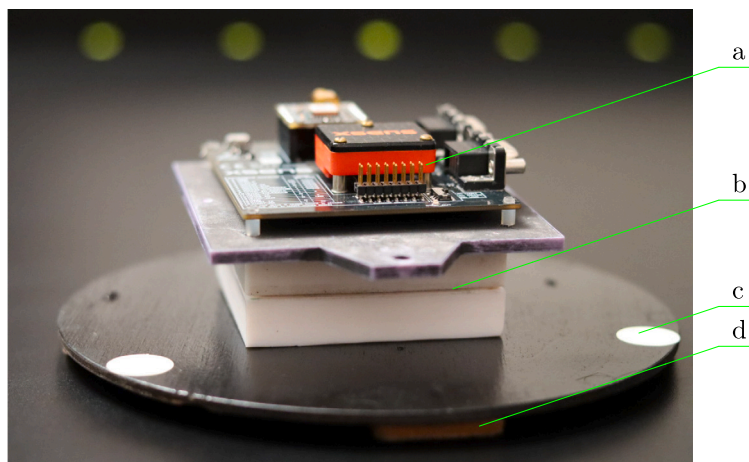


Fig. 5. The mobile measurement platform: a — sensor module (Xsens MTi-630), b — vibration isolation, c — photoluminescent marker, d — low-friction fabric.

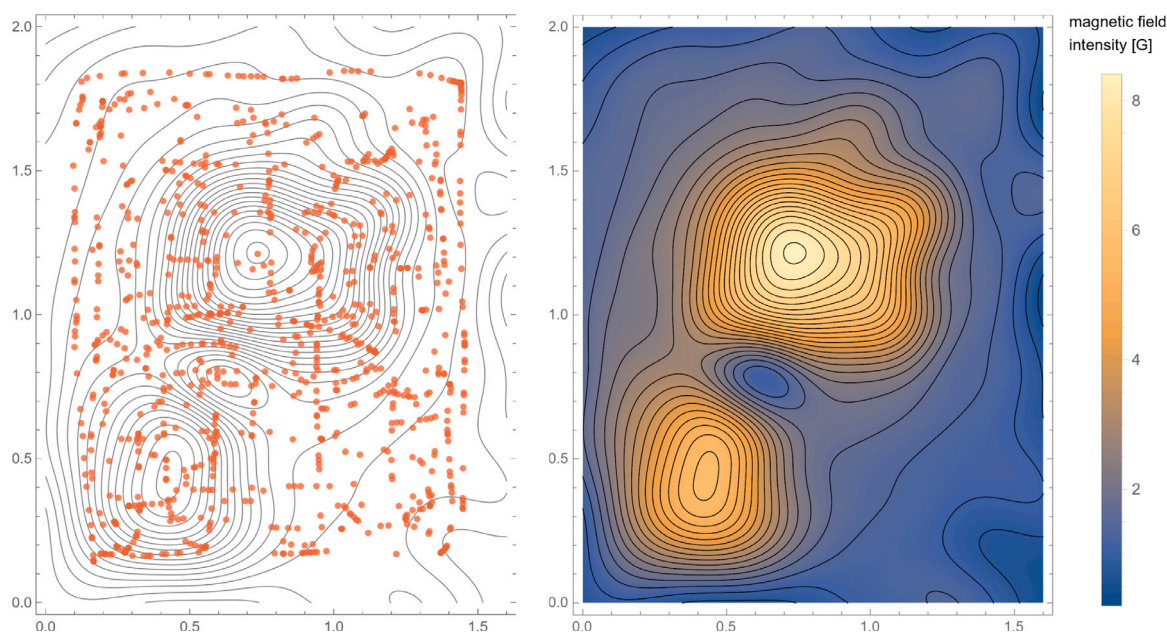


Fig. 6. Measurement points used for mapping the magnetic field on the experimental stand of dimensions  $1.6 \times 2.0$  [m] (left). Mapped magnetic field intensity (right).

Section 2.3.2. To account for the randomness of the simulated measurement noise, a Monte Carlo approach was used, with 10,000 correction procedures performed for each trajectory.

The means of the corrected trajectories  $\mu_{Z_t}$  are plotted in Fig. 7 using green lines. The mean localization errors for the entire corrected trajectories A and B are 4.9 cm and 4.0 cm, respectively, significantly lower than the mean error of 11.9 cm for the IMU-based trajectory. The time evolution of the mean localization errors in successive time steps is plotted in Fig. 8 (left), along with their  $\pm 1\sigma$  bands. Histograms of the mean localization errors for all 10,000 realizations are shown in Fig. 8 (right).

The proposed correction procedure, based on magnetometric measurements, significantly decreased the localization error, both globally (for the entire trajectories) and locally (in almost all time steps). The difference in correction accuracy between the two considered trajectories is related to their specific placement within the magnetic field and the fact that magnetometric measurements can decrease the localization uncertainty only across the isolines of the magnetic field, but not along them (see Fig. 2). This fact can be confirmed by decomposing the localization error in each time step into a sum of errors along the gradient and along the isoline. The mean absolute values of these

errors, parameterized by time  $t$ , are plotted in the top row of Fig. 9. The proposed correction procedure significantly reduced the range of the mean absolute errors along the horizontal axis, which corresponds to the direction of the gradient. In contrast, the error range along the vertical axis (along the isolines) was less affected.

The correction steps performed at a single time instant  $t$  are illustrated for trajectory A. The bottom right plot in Fig. 9 shows the entire trajectories: reference (black), IMU-based (red), and mean corrected (green). A single time step (time step No. 307) is selected, with the corresponding trajectory points explicitly marked. The bottom left plot in Fig. 9 is an inset corresponding to the area around these locations. The IMU-based location, marked “1” (red), is relatively far from the actual reference location “r” (black). The correction procedure was performed in three following steps, formally defined in Table 2:

- (1°) The corrected location  $Z_{t-1}$  from the previous time step, marked with a small green dot, was shifted by  $\Delta X_t$  to obtain the location  $Y_t$ , marked “2”.
- (2°) The locations  $Y_t$  (“2”) and IMU-based  $X_t$  (“1”) were used to obtain the location  $\bar{Z}_t$  (“3”). This location lies on a different isoline of the magnetic field than the actual reference location “r”.

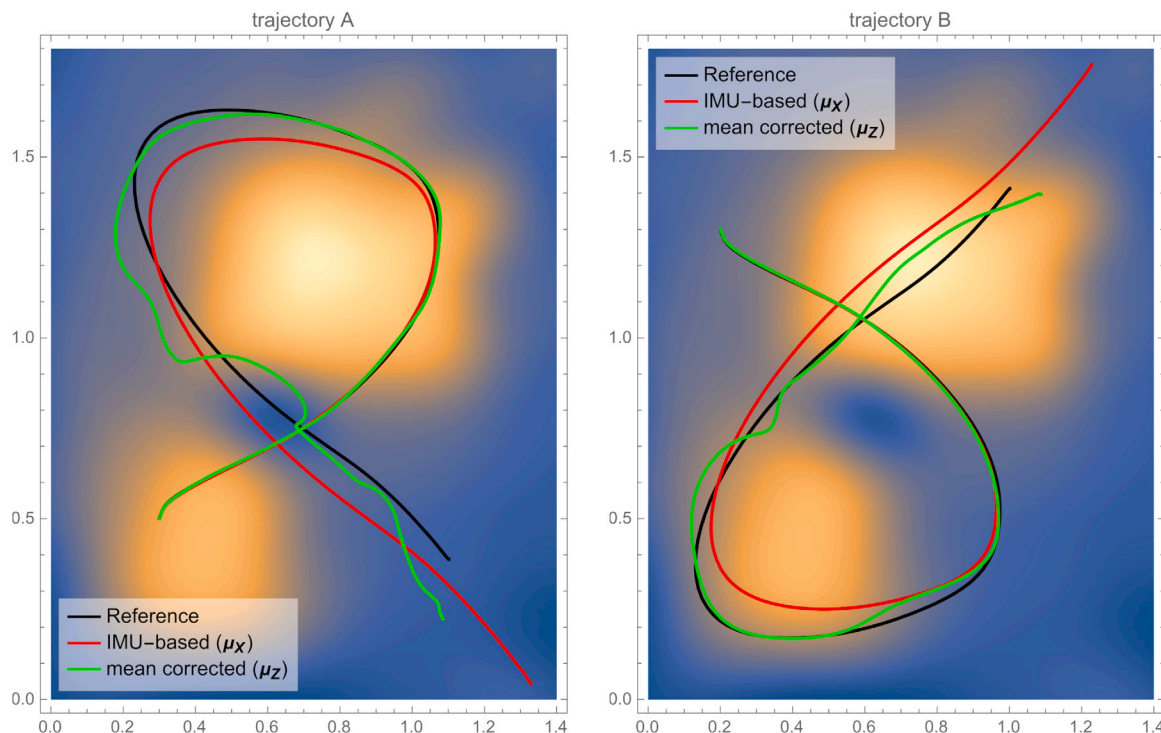


Fig. 7. The bow-shaped trajectory of the mobile platform (trajectory A, left) and its vertical flip (trajectory B, right). The actual reference, IMU-reported  $X_i$ , and mean corrected  $Z_i$  trajectories are plotted in black, red, and green, respectively.

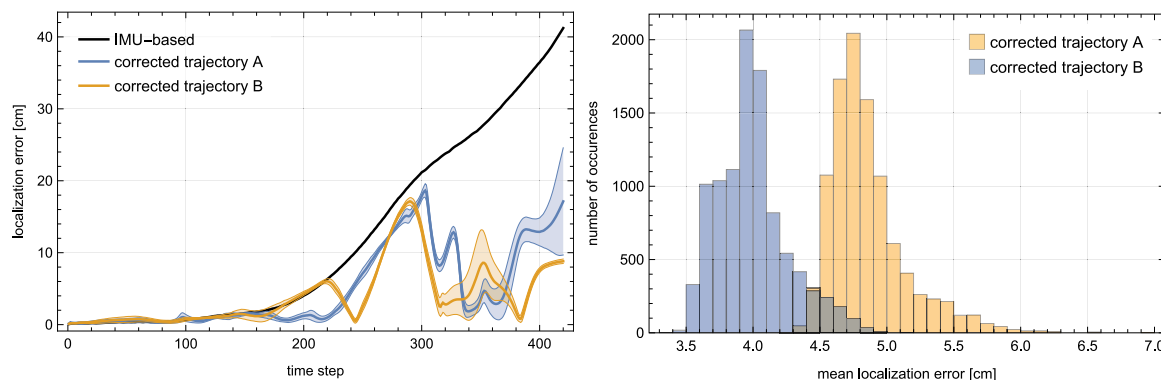


Fig. 8. (left) Localization error in successive time steps for the IMU-based and two corrected trajectories: mean values and  $\pm 1\sigma$  bands. (right) Histogram of the mean localization error for the two corrected trajectories.

(3<sup>o</sup>) The location  $\bar{Z}_i$  (“3”) was updated using the magnetic field measurement to obtain the final corrected location  $Z_i$  (“4”). The update pushed the location towards the proper isoline (that of the reference location “r”), which is emphasized by means of the light gray shading.

The corrected trajectory (“1”) slides across the magnetic field isolines similarly to the reference trajectory (“r”). However, magnetic field measurements cannot provide information about the location component along the isolines, which thus remains influenced by the error of the IMU-based localization system.

### 4.3. Comparison with a particle filter approach

To confirm the performance of the developed method, the results obtained in Section 4.2 were compared with those acquired using a particle filter. Particle filters have been extensively studied in the context of magnetic anomaly-based positioning and navigation (see, for example, [52–54]). The particle filter was implemented in its standard

version, following the algorithm outlined in [52], which relies on three major steps: (1) calculation of weights, proportional to the measurement density; (2) resampling, which discards less significant particles and generates new ones; and (3) position updating of samples using a propagation model. To ensure a consistent comparison, the particle filter was provided with the same data as the Bayesian correction approach, including an identical magnetic anomaly field map, magnetic measurement noise for particle weight updating, and IMU-based data for particle propagation modeling. Furthermore, 1000 particles were used to estimate the initial position, distributed according to a normal distribution centered around the starting position with a standard deviation of 5 cm. At each step, resampling was performed by discarding particles with normalized weights below 0.9, followed by the generation of new particles according to a normal distribution centered around the remaining particles with a standard deviation of 3 cm. Additionally, the total number of particles was constrained to vary between 100 and 3000.

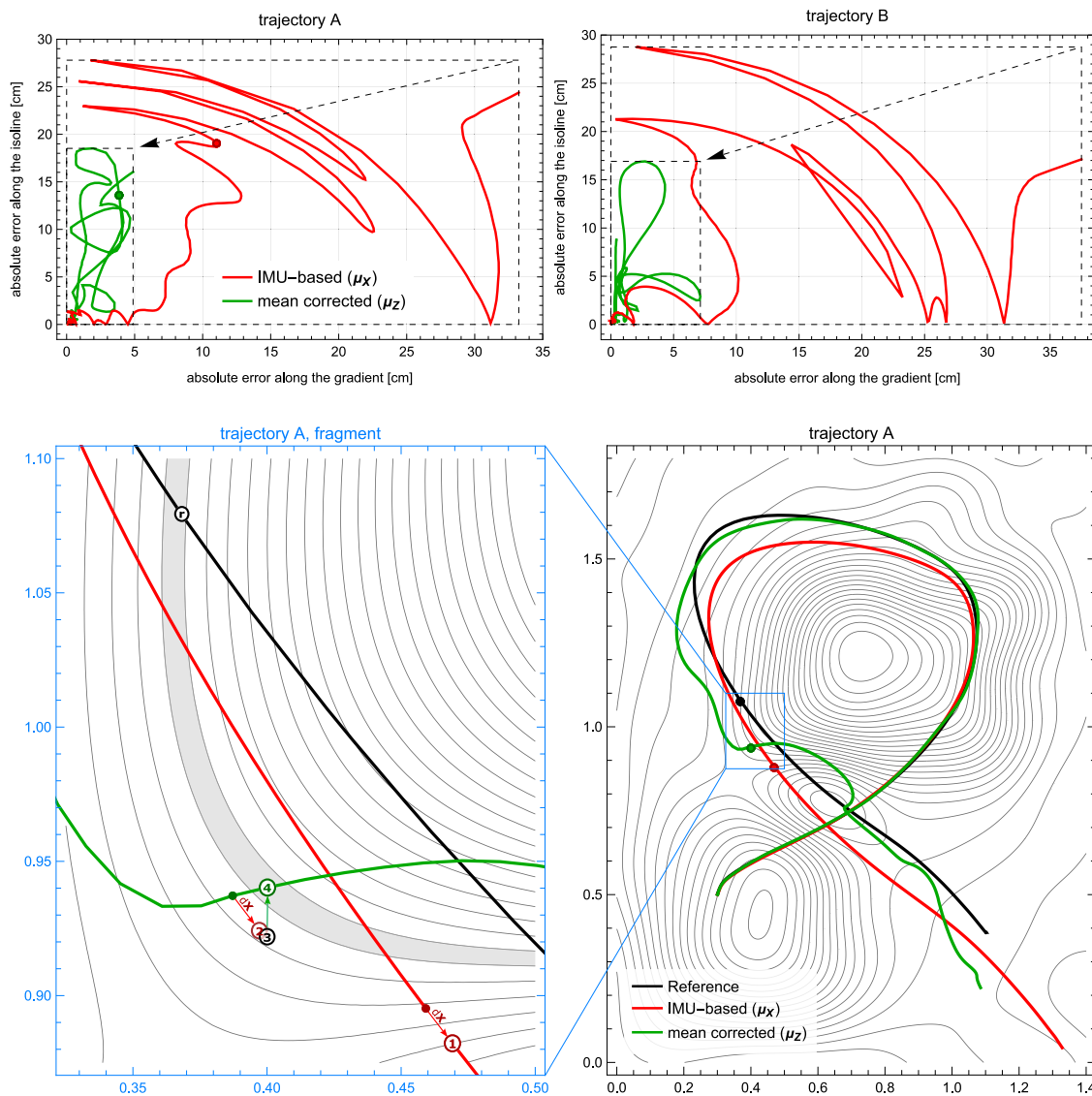


Fig. 9. (top) Decomposition of the mean absolute localization error, in successive time steps, into components along the local isoline and along the local gradient for the corrected trajectories A and B. (bottom) The reference, IMU-based, and mean corrected trajectory A. The bottom left inset illustrates the correction procedure performed in a single time step.

Fig. 10 compares the localization errors of both approaches. In terms of the overall positioning accuracy, the proposed Bayesian correction is slightly outperformed by the particle filter. As listed in Table 3, the particle filter reduced the mean error value by 8.2 mm (16.9%) for trajectory A and by 2.4 mm (6.0%) for trajectory B. Nevertheless, several advantages of the proposed Bayesian correction can be observed and summarized as follows:

1. The Bayesian correction was significantly more accurate in the initial stages of both trajectories. It ensured stable and precise tracking of the actual position, while the particle filter yielded substantially larger errors due to its stochastic nature. The observed stability in position estimation with the Bayesian correction during the initial phase may offer advantages in scenarios involving temporary losses of GPS signals.
2. The stochastic characteristics of the particle filter are emphasized in trajectory A, where significant variation of the estimated position can be observed in the second stage of the trajectory (much larger than for the Bayesian correction). This indicates that the expected performance of the particle filter may not always be guaranteed, as evidenced by the very large values

of standard deviation in Table 3 and the broad error histogram shown in Fig. 11.

3. The intrinsic randomness of the particle filter makes its performance highly sensitive to the selection of algorithm parameters, particularly in the resampling step. The choice of appropriate thresholds for discarding the least significant particles and distributions for generating new particles can significantly impact the precision and stability of the estimated position. In contrast, the proposed Bayesian correction approach does not require any preliminary tuning, which promotes reliability and simplifies implementation.
4. Real-time implementations of the Bayesian correction are facilitated by its minimal computational cost. As listed in Table 2, the average processing time for one iteration of the developed Bayesian algorithm was 3.16 ms (using a standard PC running Windows OS). In contrast, one iteration of the particle filter required 1.34 s on average (over 400 times longer). This significant difference (2–3 orders of magnitude) is mainly due to the repetitive generation of random distributions and multiple readings of the magnetic field map.

**Table 3**  
Localization errors for the Bayesian correction procedure and the particle filter: mean trajectory error and its  $\pm 1\sigma$  value. Mean processing time per single iteration.

	trajectory A mean error $\pm 1\sigma$ [cm]	trajectory B mean error $\pm 1\sigma$ [cm]	mean processing time per iteration
Bayesian correction	$4.85 \pm 0.29$	$4.00 \pm 0.26$	3.16 ms
particle filter	$4.03 \pm 1.28$	$3.76 \pm 0.20$	1.34 s

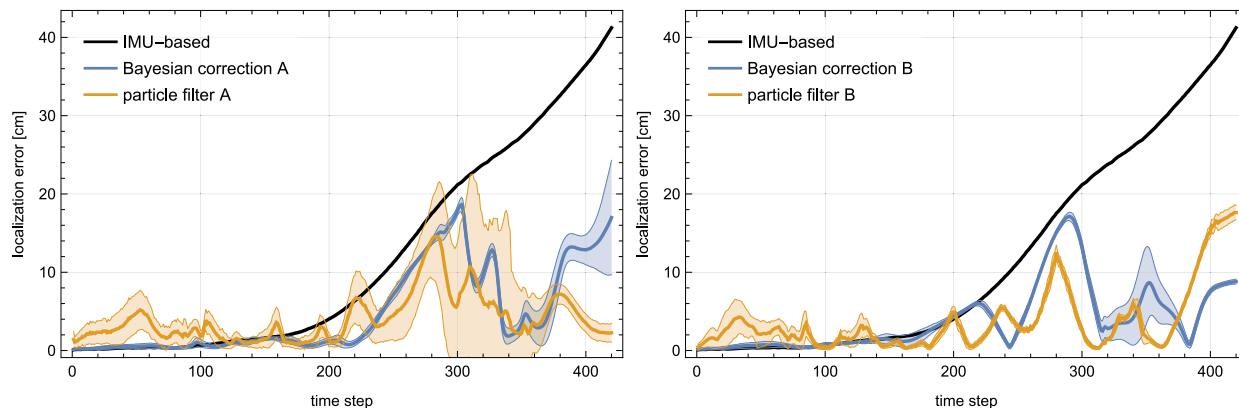


**Fig. 10.** Localization errors in successive time steps and their  $\pm 1\sigma$  bands for: (left) trajectory A; (right) trajectory B. The curves correspond to the IMU-based trajectory, trajectory corrected using the proposed Bayesian approach, and particle-filtered trajectory.

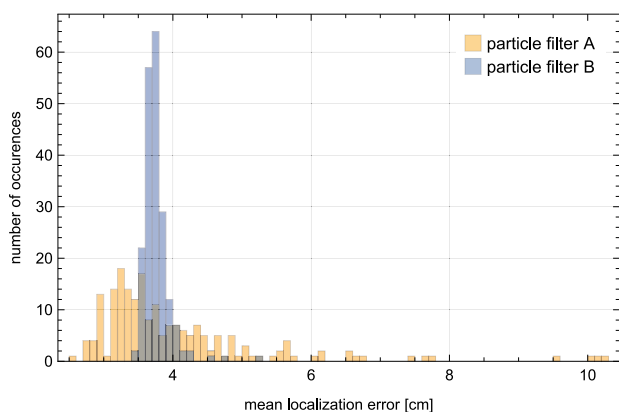


**Fig. 11.** Histogram of the mean localization error for the two particle-filtered trajectories (to be compared with Fig. 8).

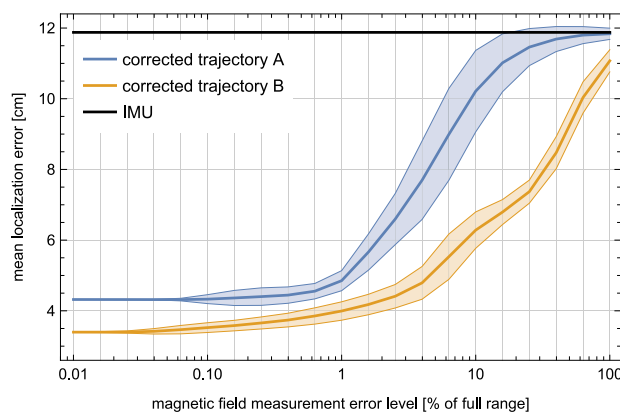


**Fig. 12.** Dependence of mean absolute localization errors and their  $\pm 1\sigma$  bands on the rms measurement error level of the magnetometer, expressed in terms of the full range of the magnetic field. The black horizontal line marks the localization error of the IMU-based trajectory.

#### 4.4. Sensitivity to measurement error of the magnetometer

An important factor in the proposed Bayesian correction procedure is the measurement error level of the magnetometer. This error affects the accuracy of the measurements and is accounted for in the coefficient  $\sigma_M$ . The examples in the preceding Section 4.2 involved a measurement error at the rms level of 1% of the full magnetic field range, which conservatively overestimated the actual measurement error of the employed physical magnetometer. In practical applications, the measurement error, expressed in relative terms of the field range, can vary considerably. This variation can be due to either a small range of the magnetic field in the area of interest or the physical limitations of the sensor. This section tests the efficiency of the proposed method under different measurement error levels. Fig. 12 plots the mean absolute localization errors for both considered trajectories (A and B), together with their  $\pm 1\sigma$  bands, in dependence on the measurement error ranging from 0.1% up to 100% of the full field range. The horizontal axis is plotted in a logarithmic scale. As in Section 4.2, the value of  $\sigma_M$  used in computations was additionally increased by 5% to account for magnetic map inaccuracies and field linearization errors.

For large measurement noise levels, the mean localization error approaches that of the IMU-based trajectory. This outcome is intuitive, as magnetic field measurements with large errors do not provide meaningful information for correcting localization. The localization error is low and relatively stable for measurement noise up to at least 1% rms, which represents a noise level an order of magnitude larger than that of the sensor used in the experiment.

#### 5. Conclusion

This paper presents a new method for real-time localization of an object traveling in a GPS-denied environment. Based on Bayesian formalism, the method utilizes measurements of magnetic field anomalies. In contrast to other commonly used localization methods, such as those relying on particle filters, the developed approach eliminates the need for an iterative procedure, enabling real-time implementation regardless of the scale of the designated area. The instantaneous operation of the algorithm is well-suited for precise position correction during temporary losses of GPS signal.

Experimental validation confirmed the effectiveness of the proposed algorithm in utilizing magnetic field measurements to refine the initial position obtained from the IMU module. The correction method demonstrated a substantial 58%–67% improvement in the mean position error compared to the IMU-derived position estimates. Further analysis confirmed the robustness of the proposed method to magnetic field measurement errors. A comparison to a particle filter approach revealed a significant improvement in both computational efficiency (by 2–3 orders of magnitude) and error stability, albeit at the cost of a slightly decreased positioning accuracy (by 6%–17%).

Simultaneously, certain limitations of the method were identified. In particular, it was observed that the correction of position is significantly more effective along the direction of the magnetic field gradient. It suggests that proper trajectory planning can increase the accuracy of magnetic localization. Moreover, the experimental validation was performed in laboratory conditions. Further steps towards real-world applications will involve significant new challenges related to the magnetic disturbances and the dynamic variability of the magnetic field.

### CRedit authorship contribution statement

**Łukasz Jankowski:** Investigation, Formal analysis, Conceptualization, Methodology, Software, Validation, Visualization, Writing – original draft, Writing – review & editing. **Dominik Pisarski:** Conceptualization, Data curation, Formal analysis, Investigation, Methodology, Software, Validation, Visualization, Writing – original draft, Writing – review & editing. **Robert Konowrocki:** Writing – review & editing, Writing – original draft, Visualization, Software, Resources, Data curation, Investigation, Methodology. **Błażej Popławski:** Writing – review & editing, Writing – original draft, Methodology, Investigation. **Rami Faraj:** Visualization, Supervision, Resources, Project administration, Methodology, Investigation, Funding acquisition, Conceptualization, Writing – original draft, Writing – review & editing.

### Declaration of competing interest

The authors declare that they have no known competing financial interests or personal relationships that could have appeared to influence the work reported in this paper.

### Data availability

The data is available on request from the corresponding author, pending approval by the Institute of Fundamental Technological Research, Polish Academy of Sciences.

### Declaration of Generative AI and AI-assisted technologies in the writing process

During the preparation of this work the authors used Grammarly, ChatGPT, and Google Translate in order to correct language, grammar, and punctuation of the text. After using these tools, the authors reviewed and edited the content as needed and take full responsibility for the content of publication.

### Acknowledgments

This research was funded by the National Centre for Research and Development (NCBR), Poland, under the grant agreement DOB-SZAFIR/01/B/018/04/2021.

### References

- [1] S. Nirjon, J. Liu, G. DeJean, B. Priyantha, Y. Jin, T. Hart, COIN-GPS: indoor localization from direct GPS receiving, in: Proceedings of the 12th Annual International Conference on Mobile Systems, Applications, and Services, ACM, Bretton Woods New Hampshire USA, 2014, pp. 301–314, <http://dx.doi.org/10.1145/2594368.2594378>.
- [2] N. Crocetto, F. Pingue, S. Ponte, G. Pugliano, V. Sepe, Ionospheric error analysis in GPS measurements, *Ann. Geophys.* 51 (4) (2008) 585–595, <http://dx.doi.org/10.4401/ag-4456>.
- [3] B. Van Den Bergh, S. Pollin, Keeping UAVs under control during GPS jamming, *IEEE Syst. J.* 13 (2) (2019) 2010–2021, <http://dx.doi.org/10.1109/JSYST.2018.2882769>.
- [4] A.J. Kerns, D.P. Shepard, J.A. Bhatti, T.E. Humphreys, Unmanned aircraft capture and control via GPS spoofing, *J. Field Robotics* 31 (4) (2014) 617–636, <http://dx.doi.org/10.1002/rob.21513>.
- [5] J. Enright, T. Barfoot, M. Soto, Star tracking for planetary rovers, in: 2012 IEEE Aerospace Conference, IEEE, Big Sky, MT, 2012, pp. 1–13, <http://dx.doi.org/10.1109/AERO.2012.6187042>.
- [6] R. Bloudicek, P. Makula, J. Bajer, M. Svarc, Possibilities of hyperbolic navigation during the approach to landing phase, in: 2016 IEEE/AIAA 35th Digital Avionics Systems Conference (DASC), IEEE, Sacramento, CA, USA, 2016, pp. 1–6, <http://dx.doi.org/10.1109/DASC.2016.7778087>.
- [7] A. Cesetti, E. Frontoni, A. Mancini, P. Zingaretti, S. Longhi, A vision-based guidance system for UAV navigation and safe landing using natural landmarks, *J. Intell. Robot. Syst.* 57 (1–4) (2010) 233–257, <http://dx.doi.org/10.1007/s10846-009-9373-3>.
- [8] B. Sinopoli, M. Micheli, G. Donato, T. Koo, Vision based navigation for an unmanned aerial vehicle, in: Proceedings 2001 ICRA. IEEE International Conference on Robotics and Automation (Cat. No.01CH37164), 2, IEEE, Seoul, South Korea, 2001, pp. 1757–1764, <http://dx.doi.org/10.1109/ROBOT.2001.932864>.
- [9] G. Conte, P. Doherty, Vision-based unmanned aerial vehicle navigation using geo-referenced information, *EURASIP J. Adv. Signal Process.* 2009 (1) (2009) 387308, <http://dx.doi.org/10.1155/2009/387308>.
- [10] J. Courbon, Y. Mezouar, N. Guénard, P. Martinet, Vision-based navigation of unmanned aerial vehicles, *Control Eng. Pract.* 18 (7) (2010) 789–799, <http://dx.doi.org/10.1016/j.conengprac.2010.03.004>.
- [11] E. Metzger, Recent gravity gradiometer developments, in: Guidance and Control Conference, American Institute of Aeronautics and Astronautics, Hollywood, FL, U.S.A, 1977, pp. 306–315, <http://dx.doi.org/10.2514/6.1977-1081>.
- [12] R.E. Bell, Gravity gradiometry, *Sci. Am.* 278 (6) (1998) 74–79.
- [13] C. Affleck, A. Jircitano, Passive gravity gradiometer navigation system, in: IEEE Symposium on Position Location and Navigation. a Decade of Excellence in the Navigation Sciences, IEEE, Las Vegas, NV, USA, 1990, pp. 60–66, <http://dx.doi.org/10.1109/PLANS.1990.66158>.
- [14] J. Richeson, D. Pines, GPS denied inertial navigation using gravity gradiometry, in: AIAA Guidance, Navigation and Control Conference and Exhibit, American Institute of Aeronautics and Astronautics, Hilton Head, South Carolina, 2007, pp. 1–23, <http://dx.doi.org/10.2514/6.2007-6791>.
- [15] T.C. Welker, M. Pachter, R.E. Huffman, Gravity gradiometer integrated inertial navigation, in: 2013 European Control Conference, ECC, IEEE, Zurich, 2013, pp. 846–851, <http://dx.doi.org/10.23919/ECC.2013.6669109>.
- [16] X. Wang, C. Gilliam, A. Kealy, J. Close, B. Moran, Probabilistic map matching for robust inertial navigation aiding, *NAVIGATION: J. Inst. Navig.* 70 (2) (2023) <http://dx.doi.org/10.33012/navi.583>, navi.583.
- [17] J.B. Lee, Falcon gravity gradiometer technology, *Explor. Geophys.* 32 (3–4) (2001) 247–250, <http://dx.doi.org/10.1071/EG01247>.
- [18] M.H. Dransfield, A.N. Christensen, Performance of airborne gravity gradiometers, *Leading Edge* 32 (8) (2013) 908–922, <http://dx.doi.org/10.1190/tle32080908.1>.
- [19] N. Yu, J. Kohel, J. Kellogg, L. Maleki, Development of an atom-interferometer gravity gradiometer for gravity measurement from space, *Applied Physics B* 84 (4) (2006) 647–652, <http://dx.doi.org/10.1007/s00340-006-2376-x>.
- [20] L. Wu, X. Tian, J. Ma, J. Tian, Underwater object detection based on gravity gradient, *IEEE Geosci. Remote Sens. Lett.* 7 (2) (2010) 362–365, <http://dx.doi.org/10.1109/LGRS.2009.2035455>.
- [21] H. Taheri, Z.C. Xia, SLAM; definition and evolution, *Eng. Appl. Artif. Intell.* 97 (2021) 104032, <http://dx.doi.org/10.1016/j.engappai.2020.104032>.
- [22] G. Grisetti, R. Kummerle, C. Stachniss, W. Burgard, A tutorial on graph-based SLAM, *IEEE Intell. Transp. Syst. Mag.* 2 (4) (2010) 31–43, <http://dx.doi.org/10.1109/MTS.2010.939925>.
- [23] T. Taketomi, H. Uchiyama, S. Ikeda, Visual SLAM algorithms: A survey from 2010 to 2016, *IPSN Trans. Comput. Vis. Appl.* 9 (1) (2017) 16, <http://dx.doi.org/10.1186/s41074-017-0027-2>.
- [24] A. Macario Barros, M. Michel, Y. Moline, G. Corre, F. Carrel, A comprehensive survey of visual SLAM algorithms, *Robotics* 11 (1) (2022) 24, <http://dx.doi.org/10.3390/robotics11010024>.
- [25] T. Lemaire, C. Berger, I.-K. Jung, S. Lacroix, Vision-based SLAM: Stereo and monocular approaches, *Int. J. Comput. Vis.* 74 (3) (2007) 343–364, <http://dx.doi.org/10.1007/s11263-007-0042-3>.

[26] B. Li, T. Gallagher, A.G. Dempster, C. Rizos, How feasible is the use of magnetic field alone for indoor positioning? in: 2012 International Conference on Indoor Positioning and Indoor Navigation, IPIN, IEEE, Sydney, Australia, 2012, pp. 1–9, <http://dx.doi.org/10.1109/IPIN.2012.6418880>.

[27] G. Ouyang, K. Abed-Meraim, A survey of magnetic-field-based indoor localization, *Electronics* 11 (6) (2022) 864, <http://dx.doi.org/10.3390/electronics11060864>.

[28] J. Aulinas, Y.R. Pétillet, J. Salvi, X. Lladó, The SLAM problem: a survey, in: *Artificial Intelligence Research and Development, Frontiers in Artificial Intelligence and Applications*, 2008, pp. 363–371, <http://dx.doi.org/10.3233/978-1-58603-925-7-363>.

[29] I. Vallivaara, J. Haverinen, A. Kemppainen, J. Rönning, Simultaneous localization and mapping using ambient magnetic field, in: 2010 IEEE Conference on Multisensor Fusion and Integration, IEEE, Salt Lake City, USA, 2010, pp. 14–19, <http://dx.doi.org/10.1109/MFI.2010.5604465>.

[30] X. Wang, C. Zhang, F. Liu, Y. Dong, X. Xu, Exponentially weighted particle filter for simultaneous localization and mapping based on magnetic field measurements, *IEEE Trans. Instrum. Meas.* 66 (7) (2017) 1658–1667, <http://dx.doi.org/10.1109/TIM.2017.2664538>.

[31] Y.H. Kim, H.J. Kim, J.H. Lee, S.H. Kang, E.J. Kim, J.W. Song, Sequential batch fusion magnetic anomaly navigation for a low-cost indoor mobile robot, *Measurement* 213 (2023) 112706, <http://dx.doi.org/10.1016/j.measurement.2023.112706>.

[32] A. Sheinker, B. Ginzburg, N. Salomonski, L. Frumkis, B.-Z. Kaplan, M.B. Moldwin, A method for indoor navigation based on magnetic beacons using smartphones and tablets, *Measurement* 81 (2016) 197–209, <http://dx.doi.org/10.1016/j.measurement.2015.12.023>.

[33] A. Canciani, J. Raquet, Absolute positioning using the earth's magnetic anomaly field, *NAVIGATION: J. Inst. Navig.* 63 (2) (2016) 111–126, <http://dx.doi.org/10.1002/navi.138>.

[34] A. Canciani, J. Raquet, Airborne magnetic anomaly navigation, *IEEE Trans. Aerosp. Electron. Syst.* 53 (1) (2017) 67–80, <http://dx.doi.org/10.1109/TAES.2017.2649238>.

[35] Y. Ren, L. Wang, K. Lin, H. Ma, M. Ma, Improved iterative closest contour point matching navigation algorithm based on geomagnetic vector, *Electronics (Switzerland)* 11 (5) (2022) 796, <http://dx.doi.org/10.3390/electronics11050796>.

[36] N. Xu, L. Wang, T. Wu, Z. Yao, An innovative PSO-ICCP matching algorithm for geomagnetic navigation, *Measurement* 193 (2022) 110958, <http://dx.doi.org/10.1016/j.measurement.2022.110958>.

[37] T.N. Lee, A.J. Canciani, Magslam: Aerial simultaneous localization and mapping using earth's magnetic anomaly field, *Navigation* 67 (1) (2020) 95–107, <http://dx.doi.org/10.1002/navi.352>.

[38] A. Gnadt, Machine learning-enhanced magnetic calibration for airborne magnetic anomaly navigation, in: *AIAA SCITECH 2022 Forum, American Institute of Aeronautics and Astronautics, San Diego, CA & Virtual*, 2022, pp. 1–16, <http://dx.doi.org/10.2514/6.2022-1760>.

[39] M. Kok, A. Solin, Scalable magnetic field SLAM in 3D using Gaussian process maps, in: 2018 21st International Conference on Information Fusion, FUSION, IEEE, Cambridge, United Kingdom, 2018, pp. 1353–1360, <http://dx.doi.org/10.23919/ICIF.2018.8455789>.

[40] P. Alken, E. Thebault, C. Beggan, et al., International geomagnetic reference field: the thirteenth generation, *Earth Planets Space* 73 (2021) 49, <http://dx.doi.org/10.1186/s40623-020-01288-x>.

[41] E. Le Grand, S. Thrun, 3-axis magnetic field mapping and fusion for indoor localization, in: 2012 IEEE International Conference on Multisensor Fusion and Integration for Intelligent Systems, MFI, IEEE, Hamburg, Germany, 2012, pp. 358–364, <http://dx.doi.org/10.1109/MFI.2012.6343024>.

[42] P. Robertson, M. Frassl, M. Angermann, M. Doniec, B.J. Julian, M.G. Puyol, M. Khider, M. Lichtenstern, L. Bruno, Simultaneous localization and mapping for pedestrians using distortions of the local magnetic field intensity in large indoor environments, in: *International Conference on Indoor Positioning and Indoor Navigation*, IEEE, Montbeliard, France, 2001, pp. 1–10, <http://dx.doi.org/10.1109/IPIN.2013.6817910>.

[43] A. Solin, M. Kok, N. Wahlström, T.B. Schon, S. Sarkka, Modeling and interpolation of the ambient magnetic field by Gaussian processes, *IEEE Trans. Robot.* 34 (4) (2018) 1112–1127, <http://dx.doi.org/10.1109/TRO.2018.2830326>.

[44] N. Wahlström, M. Kok, T.B. Schön, F. Gustafsson, Modeling magnetic fields using Gaussian processes, in: 2013 IEEE International Conference on Acoustics, Speech and Signal Processing, IEEE, Vancouver, Canada, 2013, pp. 3522–3526, <http://dx.doi.org/10.1109/ICASSP.2013.6638313>.

[45] R. Garnett, *Bayesian Optimization*, Cambridge, Cambridge University Press, 2023.

[46] S. Sural, A. Vadivel, A.K. Majumdar, Histogram generation from the HSV color space, in: D.B.A. M. Khosrow-Pour (Ed.), *Encyclopedia of Information Science and Technology*, first ed., IGI Global, 2005, pp. 1333–1337, <http://dx.doi.org/10.4018/978-1-59140-553-5.ch235>.

[47] H. Zhang, Y. Wu, F. Yang, Ball detection based on color information and hough transform, in: 2009 International Conference on Artificial Intelligence and Computational Intelligence, Vol. 2, 2009, pp. 393–397, <http://dx.doi.org/10.1109/AICI.2009.21>.

[48] A. Goshtasby, Image registration by local approximation methods, *Image Vis. Comput.* 6 (4) (1988) 255–261, [http://dx.doi.org/10.1016/0262-8856\(88\)90016-9](http://dx.doi.org/10.1016/0262-8856(88)90016-9).

[49] D. Brown, Decentering distortion of lenses, *Photogramm. Eng.* 32 (3) (1966) 444–462.

[50] P.R.G. Kurka, A.A. Díaz Salazar, Applications of image processing in robotics and instrumentation, *Mech. Syst. Signal Process.* 124 (2019) 142–169, <http://dx.doi.org/10.1016/j.ymsp.2019.01.015>.

[51] J.G. Fryer, D.C. Brown, Lens distortion for close-range photogrammetry, *Photogramm. Eng. Remote Sens.* 52 (1986) 51–58.

[52] A. Solin, S. Sarkka, J. Kannala, E. Rahtu, Terrain navigation in the magnetic landscape: Particle filtering for indoor positioning, in: 2016 European Navigation Conference, ENC, IEEE, Helsinki, Finland, 2016, pp. 1–9, <http://dx.doi.org/10.1109/EURONAV.2016.7530559>.

[53] H. Huang, W. Li, D.A. Luo, D.W. Qiu, Y. Gao, An improved particle filter algorithm for geomagnetic indoor positioning, *J. Sensors* 2018 (2018) <http://dx.doi.org/10.1155/2018/5989678>.

[54] B. Siebler, O. Heirich, A. Lehner, S. Sand, U.D. Hanebeck, Robust particle filter for magnetic field-based train localization, in: *Proceedings of the 35th International Technical Meeting of the Satellite Division of the Institute of Navigation (ION GNSS+ 2022)*, 2022, pp. 1849–1858, <http://dx.doi.org/10.33012/2022.18536>.